JACS
JOURNAL OF THE AMERICAN CHEMICAL SOCIETY
Article
pubs.acs.org/JACS

Structure–Property Relationship of Bifunctional MnO_2 Nanostructures: Highly Efficient, Ultra-Stable Electrochemical Water Oxidation and Oxygen Reduction Reaction Catalysts Identified in Alkaline Media

Yongtao Meng,[†] Wenqiao Song,[†] Hui Huang,[†] Zheng Ren,[‡] Sheng-Yu Chen,[†] and Steven L. Suib*[,†,‡]

[†]Department of Chemistry, University of Connecticut, 55 North Eagleville Road, Storrs, Connecticut 06269-3060, United States
[‡]Institute of Materials Science and Department of Chemicals, Materials & Biolmolecular Engineering, University of Connecticut, 91 North Eagleville Road, Storrs, Connecticut 06269-3222, United States

Supporting Information

ABSTRACT: Manganese oxides of various structures (α-, β-, and δ-MnO_2 and amorphous) were synthesized by facile methods. The electrocatalytic properties of these materials were systematically investigated for catalyzing both oxygen evolution reaction (OER) and oxygen reduction reaction (ORR) in alkaline media. Extensive characterization was correlated with the activity study by investigating the crystal structures (XRD, HRTEM), morphologies (SEM), porosities (BET), surfaces (XPS, O_2-TPD/MS), and electrochemical properties (Tafel analysis, Koutechy–Levich plots, and constant-current electrolysis). These combined results show that the electrocatalytic activities are strongly dependent on the crystallographic structures, and follow an order of α-MnO_2 > AMO > β-MnO_2 > δ-MnO_2. Both OER studies and ORR studies reveal similar structure-determined activity trends in alkaline media. In the OER studies, α-MnO_2 displays an overpotential of 490 mV compared to 380 mV shown by an Ir/C catalyst in reaching 10 mA cm^{-2}. Meanwhile, α-MnO_2 also exhibits stability for 3 h when supplying a constant current density of 5 mA cm^{-2}. This was further improved by adding Ni^{2+} dopants (ca. 8 h). The superior OER activity was attributed to several factors, including abundant di-μ-oxo bridges existing in α-MnO_2 as the protonation sites, analogous to the OEC in PS-II of the natural water oxidation system; the mixed valencies (AOS = 3.7); and the lowest charge transfer resistances (91.8 Ω, η = 430 mV) as revealed from *in situ* electrochemical impedance spectroscopy (EIS). In the ORR studies, when reaching 3 mA cm^{-2}, α-MnO_2 shows 760 mV close to 860 mV for the best ORR catalyst (20% Pt/C). The outstanding ORR activity was due to the strongest O_2 adsorption capability of α-MnO_2 suggested by temperature-programmed desorption. As a result, this discovery of the structure-related electrocatalytic activities could provide guidance in the further development of easily prepared, scalable, and low-cost catalysts based on metal oxides and their derivatives.

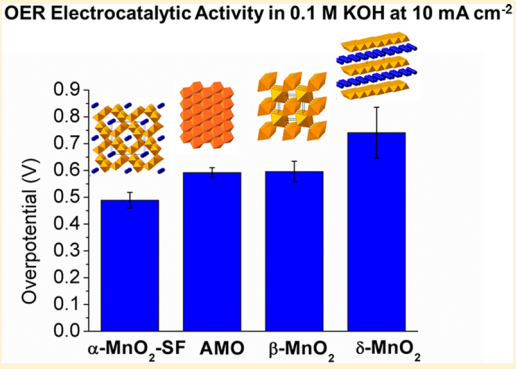

1. INTRODUCTION

Increasing energy consumption requires new energy resources and coupled storage techniques to substitute for fossil fuels such as coal, natural gas, and petroleum. Hydrogen production and carbon dioxide reduction driven by solar energy have become ultimate goals for realizing fuel production through the use of electrons and protons as reducing agents.[1−4] Water upon oxidation can provide abundant protons and electrons acting as an excellent reducing agent. Water oxidation becomes the key in solar fuel production to meet our exponentially increasing rates of consumption.[5] However, water oxidation is thermodynamically unfavorable and requires high energy input:[6]

$$2H_2O(l) \rightarrow O_2(g) + 2H_2(g) \qquad \Delta H = 572 \text{ kJ mol}^{-1} \tag{1}$$

$$2H_2O(l) \rightarrow O_2(g) + 4H^+ + 4e^- \tag{2}$$

$$4H^+ + 4e^- \rightarrow 2H_2(g) \tag{3}$$

$$E^\circ(O_2/H_2O) = 1.23 \text{ V versus RHE}$$

To facilitate water oxidation, growing efforts have been made to develop efficient, robust, and inexpensive catalysts.[2,3] Although precious metal oxides such as ruthenium and iridium oxides show the best oxygen evolution reaction (OER) activities, their scarcity and high costs hinder scalable applications.[2,7] Inspired by findings in the oxygenic photosystem II (PS-II) in nature, which is composed of Mn_4O_4Ca as the core of its catalytic center surrounded by ample proteins,[8,9] progress has been made in mimicking this unique cubane-like structure utilizing manganese oxides.[10−14] As one of the

Received: May 28, 2014
Published: July 24, 2014

   dx.doi.org/10.1021/ja505186m | J. Am. Chem. Soc. 2014, 136, 11452−11464

naturally abundant elements of low toxicity, manganese was thus highlighted as one of the most attractive candidates to meet goals of artificial synthesis and has captured the attention of researchers.[15] Manganese oxides have more than 20 polymorphs, and their multivalent nature and nonstoichiometric composition make them more complicated than simple oxides.[16] The catalytic activities of manganese oxides rely heavily on their chemical compositions and crystallographic structures, as well as morphologies and pore structures.[17−22]

Previously, manganese oxides deposited by electrochemical cycling showed high activities of OER in alkaline solution (0.1 M KOH) by matching 10 mA cm^{-2} with an overpotential of 540 mV.[2] In addition, the same MnO_x film displayed superior oxygen reduction reaction (ORR) activity.[2] The authors attributed this to structural changes (partial Mn^{III} to Mn^{IV}) of the as-prepared film introduced by the potential bias during electrolysis.[23] Bergmann et al. established a structure−activity relationship through studies of δ-MnO_2-like (layered) and β-MnO_2-like (tunneled) manganese oxides.[22] Tunnel structures were proven to have higher intrinsic activities over layered materials, considering the accessibility of water and the defects offered by these two systems.[22] Nanoparticulate β-MnO_2 prepared by screen printing was reported to reach 10 mA cm^{-2} at an overpotential of 550 mV in OER,[3] on par with the performance of the aforementioned MnO_x films.[2,3] δ-MnO_2 was also reported but with a low TOF (turnover frequency) on the order of 10^{-5} s^{-1} per Mn in a photocatalytic water oxidation system utilizing $Ru^{2+}(bpy)_3$ (a visible light sensitizer) and $S_2O_8^{2-}$ (a sacrificial agent).[24] Most studies dealt with one or two manganese oxide structures, and photochemical water oxidation reactions were widely performed to characterize the activities. The TOF ranges from 5×10^{-6} to 2×10^{-3} s^{-1} over manganese oxide complexes reported in recent studies.[3,15] Jiao et al. have studied α-MnO_2 and β-MnO_2 in photocatalytic water oxidation, in which the crystal structures and morphologies have less effect on activity than surface areas.[25] Najafpour et al.[10] described the surface area of $CaMnO_4 \cdot H_2O$ and α-Mn_2O_3 as having a "marginal effect" in contrast to an effect that stems from the unique structural motifs with appreciable bonding of water, di-μ-oxo bridging sites, feasible valences of Mn (20% Mn^{III}/Mn^{IV}, AOS = 3.8), and structural defects (low order).[26] All of these reported data were based on photocatalysis in either mildly acidic or neutral conditions with quite low efficiency[25] and suffered from the material dissolving in the buffer,[27] which makes a systematic comparison of catalysts difficult. Many manganese oxide films have been prepared and studied in EC (electrochemical) water oxidation, showing the feasibility of EC in studying film catalysts;[28,29] thus, an activity comparison can be readily realized.[2,27] The most active MnCat film catalyst suffers a dissolution issue in phosphate buffer.[27] In terms of reaction conditions, a clear pH effect on the OER has been established in electrochemical OER showing that a higher pH of >9 is favored to stabilize Mn^{3+} and, as a result, the overpotential could be lowered.[30] Under these conditions, establishing a structure−OER activity relationship and investigating their long-term stabilities which are absent in the EC system are critical.[22,26,27] In addition, ORR is the ubiquitous cathode reaction in energy storage devices such as fuel cells and metal−air batteries. ORR is also the rate limiting process of these devices due to sluggish kinetics.[31−34] Manganese oxides of diverse structures have already shown structure dependent ORR activities,[19,35] and bifunctional catalysts can be achieved after screening the structures in both OER and ORR, leading to new energy storage devices such as regenerative fuel cells[36] and rechargeable metal−air batteries.[37−40]

Less ordered amorphous manganese oxides (AMO) have the best water oxidation activity, better than octahedral molecular sieves (OMS-2, with 2 × 2 tunnel structure), analogous to the mineral cryptomelane with an α-MnO_2 structure and an octahedral layered material (OL-1, birnessite).[1] The OER has been studied in both chemical (Ce^{4+}/Ce^{3+} (E° = +1.7 V)) and photochemical systems ($Ru(bpy)_3^{3+}/Ru(bpy)_3^{2+}$ (E° = +1.24 V)). The activities reflected by the large TON shed light on the kinetics of OER, and the outstanding properties of OER were attributed to oxygen defects in the AMO.[1] Here, we systematically studied the OER and ORR activities for different MnO_x structures of δ-MnO_2 (layered) and β-MnO_2 and α-MnO_2 (various tunnel sizes), and the AMO catalysts in the EC system including their stability in catalyzing both processes. Discovering bifunctionalities of various manganese oxide structures that have not yet been reviewed and gaining insight into structure related EC activities by using various characterization techniques including XRD, SEM, TEM, EDX, XPS, EIS, TPD, CV and RDEV, and constant current electrolysis are sought in this work. Results show activities for OER and ORR are both associated with crystallographic structures, and depend highly on their intrinsic properties such as the number of deprotonation sites, mixed valences, ionic and charge transfer resistances, and adsorption abilities of O_2 (ORR).

2. RESULTS

2.1. Structure Determination, Morphology, Composition, and Porosity Characterization. Manganese oxides have very diverse structures, depending on the connectivity between the $[MnO_6]$ units via sharing corners or edges. The most common ones include the layered material δ-MnO_2, which has MnO_6-shared edges in each layer with cations such as Li^+, Na^+, and K^+ and other alkaline metals and water molecules occupying the space between the layers. Tunnel structures or so-called one-dimensional MnO_2 have many structures when the tunnel sizes vary, which include β-MnO_2 (1 × 1), γ-MnO_2 (1 × 2 and 1 × 1), α-MnO_2 (2 × 2), OMS-1 (3 × 3), and OMS-5 (2 × 4).[17,18,42,43] Among these, α-MnO_2 has been studied most extensively due to its unique adsorption, catalytic, and oxidative properties.[17,18] In terms of their applications in electrochemical fields, a layered structure is beneficial for supercapacitors,[44] while γ-MnO_2 and α-MnO_2 are used for lithium ion batteries,[45,46] and recently for lithium−air batteries.[47−49] Although the OER stabilities of α-MnO_2 are questionable,[48] the intrinsic activity for catalyzing ORR is comparable with state-of-the-art platinum catalysts.

Here we studied the four most distinct MnO_2 structures (see Figure 1), in order to investigate the effects of structure on their electrochemical OER and ORR activities: amorphous manganese oxides (AMO) have less order and are a primary form of a birnessite phase, and they have shown remarkable photo- and chemical water oxidation performance in a previous work at pH 5−6.[1] The XRD pattern of AMO is shown in Figure 2. Three weak diffraction peaks represent the amorphous nature which is also confirmed by HRTEM. No discernible fringe lattices could be observed, apart from small plate-like domains. The morphology of AMO showed aggregated particles of less than 50 nm as revealed in SEM studies. XRD data of δ-MnO_2 showed a highly crystalline character; the diffraction pattern corresponds perfectly with birnessite MnO_2 (JCPDS No. 52-

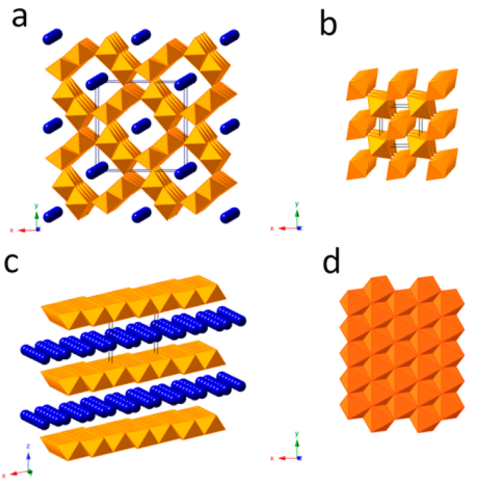

Figure 1. Structures of manganese oxide reported here in this study: (a) α-MnO_2 (2 × 2 tunnel), (b) β-MnO_2 (1 × 1 tunnel, pyrolusite), (c) δ-MnO_2 (layered, birnessite), and (d) amorphous manganese oxides (AMO).

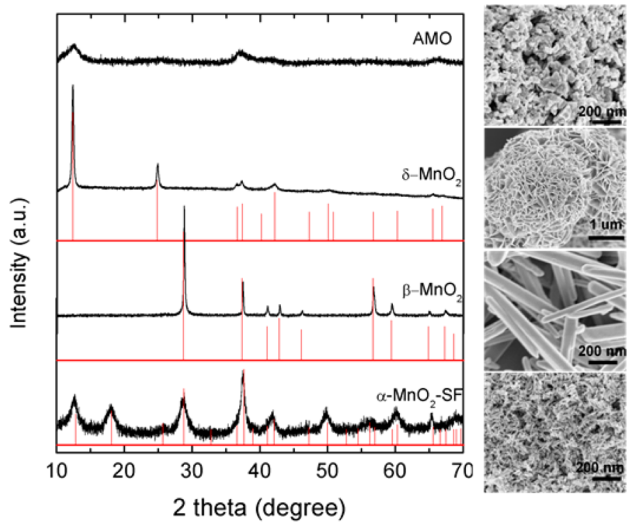

Figure 2. XRD patterns and SEM images of four manganese oxide structures, from top to bottom: AMO, δ-MnO_2 (JCPDS No. 52-0556), β-MnO_2 (JCPDS No. 24-0735), and α-MnO_2-SF (JCPDS No. 29–1020).

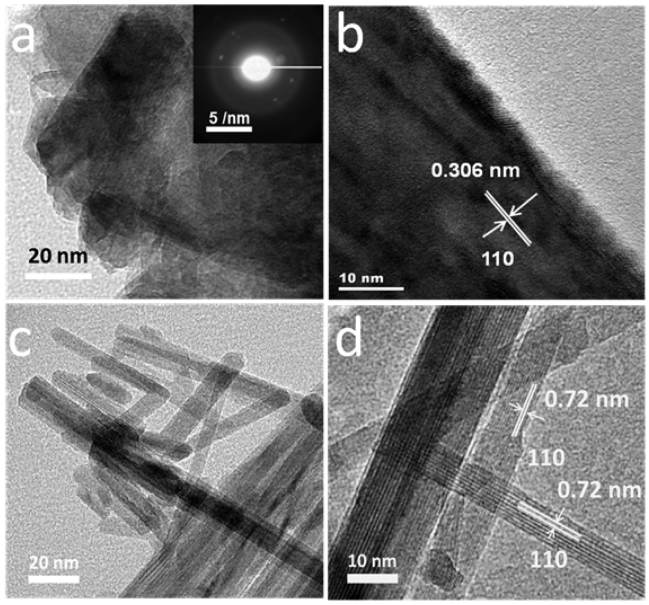

Figure 3. HRTEM images of manganese oxide nanostructures (a) AMO [the inset shows the SAED (selected area electron diffraction) pattern], (b) β-MnO_2, (c and d) α-MnO_2-SF.

0556). δ-MnO_2 exhibits a 3 μ (i.d.) sphere of nanoflowers in SEM, which is composed of thin nanoplates with dimensions of 500 nm (width) × 20 nm (thickness). The diffraction pattern of β-MnO_2 matches standard diffraction for pyrolusite (JCPDS No. 24-0735). The relatively small d spacing was confirmed by HRTEM (Figure 3) in Figure 3b; i.e., an interplanar distance of 0.306 nm corresponds to the (110) planar spacing.[50] As seen from SEM images in Figure 2, β-MnO_2 has a nanorod morphology with a 2 μ (L) × 50 nm (i.d.) dimension. The α-MnO_2-SF structure was assigned to a tetragonal cryptomelane type MnO_2 (JCPDS No. 29-1020), with lattice constants a = 9.8144 Å and c = 2.8518 Å. Accordingly, the crystalline nature of α-MnO_2-SF was also displayed in the HRTEM, which shows clear ca. 100 nm length nanofibers with about a 10 nm thickness. The uniform 0.72 nm interplanar distance corresponds to a (110) planar spacing, which suggests the material is well ordered, and the nanofiber has a preferential growth along the [001] direction which is perpendicular to the [110] direction.

The porosity information on all the synthesized materials was characterized by a N_2 sorption study, and the BET surface areas and pore volumes are presented in Table 1. AMO shows the highest BET surface area, 177 m^2/g, and a moderate pore volume, 0.27 cm^3/g, whereas α-MnO_2-SF has a smaller surface area, 112 m^2/g, but the highest pore volume, 0.48 cm^3/g. These results are comparable with our previous report on both materials.[1]

Table 1. BET Surface Area, Pore Volume, and Chemical Composition (EDX, XPS)

catalyst	BET surface area (m^2/g)	pore volume (cm^3/g)	K/Mn ratio by EDX	K/Mn by XPS
AMO	177	0.27	0.03	0.00
δ-MnO_2	26	0.16	0.29	0.28
β-MnO_2	5	0.02	0.00	0.00
α-MnO_2-SF	112	0.48	0.12	0.16
Ni/α-MnO_2-SF	147	0.40	0.12	0.11 (0.03 Ni)
α-MnO_2-HT	67	0.34	0.18 (Na/Mn)	0.17

β-MnO_2 possesses the lowest surface area, 5 m^2/g, which may be due to its smallest tunnel size (2.3 Å × 2.3 Å) as a result of the densely packed manganese octahedra. This material exhibits the lowest pore volume of 0.02 cm^3/g as well. δ-MnO_2 microspheres yield a surface area of 26 m^2/g and a pore volume of 0.16 cm^3/g, which is much lower than the previously reported value for OL-1,[1] a similarly structured material. This may be ascribed to the high crystallinity created by the hydrothermal synthesis. Our studies of highly crystalline material in this study, such as δ-MnO_2 and β-MnO_2, aim at uncovering the pure effect of structural differences on the electrochemical activities of these materials, and may on one hand provide unambiguous evidence for future material

dx.doi.org/10.1021/ja505186m | J. Am. Chem. Soc. 2014, 136, 11452–11464

research but may also guide material syntheses by using simplified routines as described in our Synthesis section.

Knowing the structure and porosity, we further studied the composition of each material, particularly the K to Mn ratio by energy dispersive X-ray (EDX) spectroscopy, in the hopes of correlating this information with the oxidation states of manganese, which has been highlighted as a key in the EC water oxidation in recent studies.[30] AMO presents the lowest K/Mn atomic ratio, leading to a high ratio of Mn^{4+}/Mn^{3+}, whereas the latter reduced ions are suggested to be the active sites in recent studies for hydrocarbon oxidation and EC water oxidation.[30,51] β-MnO_2 does not have K^+ in its structure because of its small tunnel size, which cannot accommodate any cations, and as a result, Mn^{4+} predominates in its structure. The α-MnO_2 cryptomelane (KMn_8O_{16}) shows K/Mn = 0.12, which agrees with a previous study.[1] This K/Mn ratio is close to half occupation of the tunnel sites by K^+, and corresponds to a theoretical AOS of 3.875.[32] However, the reported value is as low as 3.79,[1] which is attributed to oxygen defects in the material, and consequently, the material shows tremendous activity in many oxidation processes.[17,18] The number of Mn^{3+} ions in α-MnO_2 is thus largely increased in comparison with AMO. Although δ-MnO_2 exhibits an even larger K/Mn ratio of 0.29, agreeing with other studies,[24] this material has been studied as a WO (water oxidation) catalyst and shows low activities, and led to a different scenario in which Mn^{4+} dominates due to the involvement of oxygen-rich phases.[24] The K/Mn ratio characterized by XPS (Table 1) correlated very well with the results from EDX studies.

2.2. OER Activity for MnO_2 of Different Structures. Electrochemical water oxidation activities (Figure 4) of α-MnO_2, β-MnO_2, δ-MnO_2, and AMO were evaluated by CV utilizing a rotating disk electrode (RDE) in 0.1 M KOH, at a scan rate of 5 mV s^{-1} and a rotation rate of 1600 rpm. These conditions were widely used and are considered as general conditions in such studies to eliminate O_2 bubbles formed during the reaction, and to instantly remove the other products.[2,28]

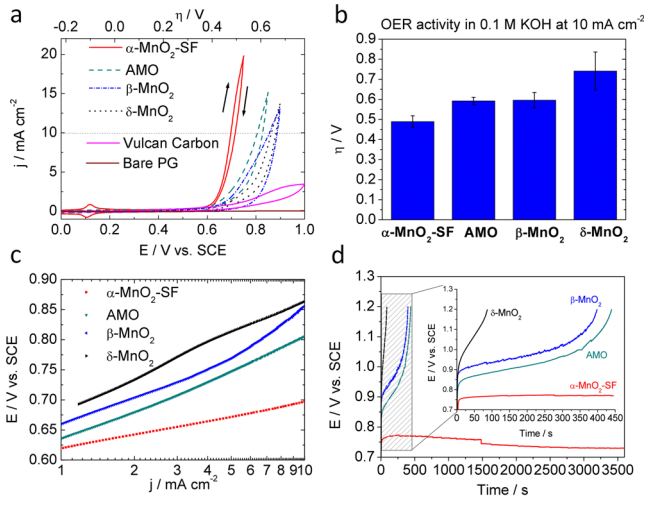

Figure 4. Electrochemical water oxidation activities of manganese oxides: (a) Rotating disk electrode voltammogram (RDEV) curves. Sweep directions are shown by arrows. (b) Comparison of overpotentials needed to reach 10 mA cm^{-2}. (c) Derived Tafel slopes from RDEV cures (anodic branches). (d) Long-term stability test carried out in 0.1 M KOH, under a constant current density of 5 mA cm^{-2} and rotation rate of 1600 rpm (the inset shows the zoomed in view of stabilities over the range 0−450 s).

The voltammograms are shown in Figure 4a. α-MnO_2 shows extraordinary activity, which demonstrates much lower overpotential needed to reach 10 mA cm^{-2}, a reference value in evaluating OER catalysts especially for a solar water splitting device which works with 10% efficiency.[2] The average overpotential for α-MnO_2 to reach this reference value is 0.49 V, compared to AMO (η = 0.59 V), β-MnO_2 (η = 0.60 V), and δ-MnO_2 (η = 0.74 V). The reported values in Figure 4b correspond to the average values calculated from the RDEV measurements based on at least three independently prepared electrode surfaces. Consequently, the error bars are shown and represent the standard deviations over three tests on each catalyst. The RDEV for α-MnO_2-SF expresses a sharp increase between 0.6 and 0.7 V (vs SCE), illustrating a faster reaction rate.[5] On the contrary, the RDEV curves for AMO, β-MnO_2, and δ-MnO_2 show a slower increase of the current densities with increasing potentials, indicating their sluggish reaction kinetics. To gain further insight into the OER activities of these manganese oxides, Tafel plots,[5,22,52] a merit of measurement to study the kinetics of OER, were retrieved from the anodic sweep of the RDEV curves and are presented in Figure 4c. A linear dependency of E vs $\log(j)$ was achieved for all the samples, and displayed with different slopes and intercepts. The Tafel slope values and specific activity data are listed in Table 2; the overall slopes follow an order of α-MnO_2-SF (77.5 mV dec^{-1}) < AMO (178.7) < β-MnO_2 (180.2) < δ-MnO_2 (188.6), with the mass activity and turnover frequency following an inverse trend. α-MnO_2-SF displays the lowest Tafel slope similar to that of the MnCat film,[27] which shows lower TOF (0.0020 vs 0.0047 s^{-1}) and one magnitude lower current density than ours. Thus, α-MnO_2-SF could potentially afford a superior OER catalyst. In contrast, the relatively lower catalytic activities for AMO, β-MnO_2, and δ-MnO_2 were shown by much higher Tafel slopes and their lower TOF, in agreement with recent OER studies on similar manganese oxide structures.[24,25] This is also embodied in the heterolysis shown by the RDEV curves that may represent the unsteady states and deteriorated stabilities caused by the inertness of such materials. Indeed, such a hypothesis was confirmed in the initially continuous three-cycle tests (see the Supporting Information). The RDEV curves for α-MnO_2-SF show a steady sharp increase for all the three cycles, and the curves almost overlap, signifying primarily high stability, in comparison to AMO, β-MnO_2, and δ-MnO_2, which suffer a drastic activity loss in the repeated cycles. For instance, AMO shows a sudden ~28.5% drop of its highest current density in the second cycle in comparison with the first cycle (shown in Figure 4a) and then another 16% drop in the third cycle compared with the second cycle. These observations may reflect the unstable nature of these catalysts in EC.

In order to further discover the stabilities of these catalysts, we carefully performed controlled current electrolysis by using the chronopotentiometry technique, and the results are shown in Figure 4d. During the test, the electrodes with catalyst coatings were maintained at a constant 5 mA cm^{-2} current density for a long period of time at a rotation rate of 1600 rpm. The potential was measured versus time, and a potential window was set for each catalyst, 0−0.75 to 1.2 V (vs SCE), since at around 0.75 V (η = 0.53 V), each catalyst could reach a current density close to 5 mA cm^{-2} predefined by Figure 4a. The upper-bound potential defines the end point of the data collection. Thus, for example, preliminary stability tests show

dx.doi.org/10.1021/ja505186m | J. Am. Chem. Soc. 2014, 136, 11452−11464

Table 2. Summary of the OER Catalytic Activities Revealed by RDEV at a Rotation Rate of 1600 rpm and a Scan Rate of 5 mV s^{-1}

catalyst	E (V)[a] at I = 10 mA cm^{-2}	Tafel slope[b] (mV dec^{-1})	mass activity at η = 0.45 V (A g^{-1})[f]	TOF at η = 0.45 V (s^{-1})[f]	reference
α-MnO_2-SF	1.72 ± 0.03	77.5	23.4	0.0047	this study
α-MnO_2-HT	1.72 ± 0.02	87.7	17.7	0.0036	this study
Ni/α-MnO_2-SF	1.74 ± 0.03	107.4	15.8	0.0032	this study
AMO	1.82 ± 0.02	178.7	8.5	0.0017	this study
β-MnO_2	1.83 ± 0.03	180.2	5.7	0.0012	this study
δ-MnO_2	1.97 ± 0.09	188.6	4.2	0.0008	this study
MnO_x film	1.77	n.a.	n.a.	n.a.	ref 2
MnCat	not reached	76−80	n.a.	0.0010[c]	ref 27
β-MnO_2 film	1.78	90−96	n.a.	0.0003[d]	ref 3
20 wt % Ir/C	1.61	n.a.	n.a.	n.a.	ref 2
20 wt % Ru/C	1.62	n.a.	n.a.	n.a.	ref 2
RuO_2	1.62	90	30.2	0.0104[e]	ref 67

[a]Potential (vs RHE) needs for reaching a current density of 10 mA cm^{-2} in electrochemical water splitting. Standard deviations were derived from three independent trails of experiments on the same catalyst, including electrode preparation and testing. [b]Tafel equation $\eta = b \log(j/j_0)$, η is the overpotential, b is the Tafel slope, j is the current density, and j_0 is the exchange current density. [c]pH 7, based on estimation. [d]pH 14, η = 0.6 V. [e]η = 0.35 V. [f]See the Experimental Section for the calculation method. "n.a." stands for data that are not available from the literature.

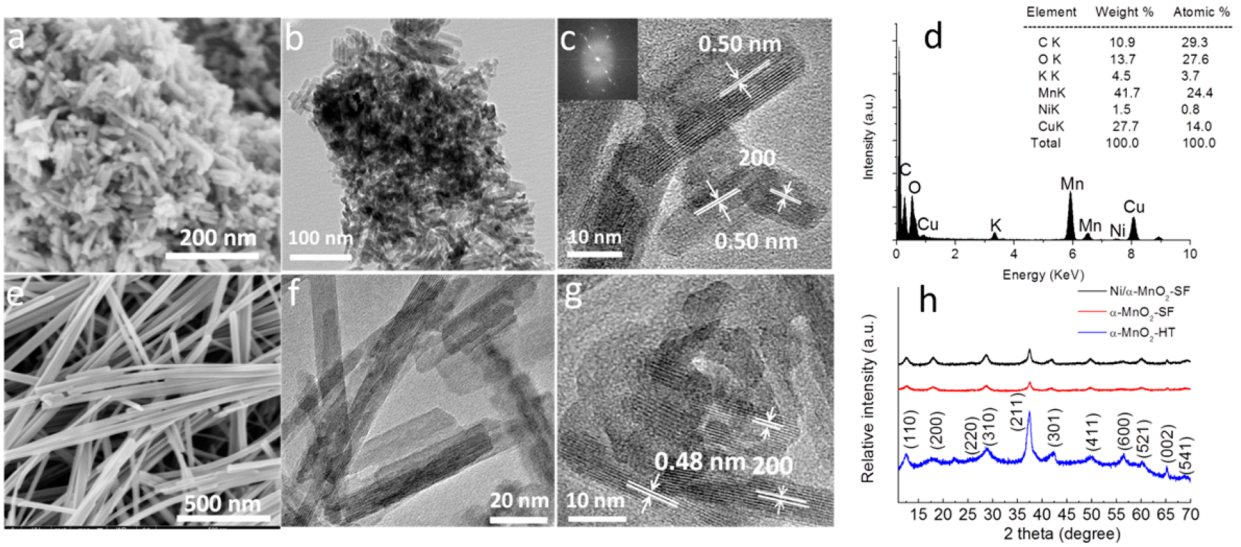

Figure 5. SEM images of (a) Ni/α-MnO_2-SF and (e) α-MnO_2-HT; TEM images for (b, c) Ni/α-MnO_2-SF and (f, g) α-MnO_2-HT; (d) EDS spectrum of Ni/α-MnO_2-SF with the elemental components and their distributions (inset); and (h) XRD patterns of α-MnO_2 (-SF, -HT, Ni/-).

AMO, β-MnO_2, and δ-MnO_2 have relatively lower stabilities in continuous electrolysis; thus, we extended the end point of the chronopotentiometry test for them to 1.2 V (1.0 V for α-MnO_2-SF) in the hope of recording longer performance data for these unstable catalysts for the purpose of facilitating the latter comparison. Figure 4d shows only the first hour of the test curve for α-MnO_2-SF, which is the most active catalyst among the four catalysts. The stability lasts as long as 3 h to reach 1 V (see details in Figure 6d). In the first hour, α-MnO_2-SF shows extremely stable performance without displaying any positive shift of the potential; after 1 h, E = 0.73 V (η = 0.52 V) as compared to the starting potential of 0.75 V. In contrast, AMO, β-MnO_2, and δ-MnO_2 appear to have inferior stabilities by reaching 1.2 V in less than 450 s, indicating severe polarization in constant current electrolysis, due to the limited number of active sites in these polymorphs. Specifically, AMO takes 440 s to reach 1.2 V, as compared to 398 s for β-MnO_2 and 87 s for δ-MnO_2, respectively. Therefore, the stabilities of these four polymorphs of manganese oxide follow the same trend as that shown in their activities: α-MnO_2-SF > AMO > β-MnO_2 > δ-MnO_2. This is the first systematic study for discovering this trend, and this finding is in line with another report.[22]

2.3. OER Activity for α-MnO_2 Prepared with Modified Methods. α-MnO_2 was prepared with a variety of methods, such as hydrothermal, reflux, solvent-free, and low temperature synthesis. The solvent-free method has shown extraordinary ORR catalytic activity in a previous study,[32] which is in line with the average oxidation state (AOS) of 3.73 offered by this method, and the high surface area (>140 m^2 g^{-1}), large pore volume, and small crystallite size.[32] All of those factors suggest that this catalyst could be a suitable candidate in electrochemical OER due to the increased number of active sites. Therefore, there is also a great need to compare the OER activities with α-MnO_2 synthesized by other means. To this end, we further synthesized α-MnO_2 by a facile hydrothermal method (see the Experimental Section). The alpha phase was confirmed by XRD diffraction and HRTEM (Figure 5h and g). The intense diffraction pattern reflects the high crystallinity, while the lattice fringes in HRTEM can be indexed as the (200)

planar spacings of α-MnO_2 (JCPDS No. 29-1020). The morphology of α-MnO_2-HT was characterized by SEM (Figure 5e) and displayed very thin (less than 50 nm) and much longer nanofibers (>5 μm, Figure S2, Supporting Information).

Another α-MnO_2 with Ni dopant was synthesized by a similar solvent-free method as α-MnO_2-SF by adding nickel nitrate. Ni^{2+} doped α-MnO_2 was reported as a superior catalyst in ORR due to the enhancement of the electrochemical activity by adjusting the charge transfer rate.[32] Applying a doubled dopant amount of Ni instead in this study, we prepared the Ni/α-MnO_2-SF to study its OER performance. EDX results (Figure 5d) confirmed the elemental compositions including Ni, Mn, and O, whereas the Cu signal stems from the TEM grids. The amount of Ni is determined to be 1.5 wt %, about half of the nominal ratio. The XRD pattern is shown in Figure 5h, which can be readily indexed as being α-MnO_2, without showing any phase change or newly evolved phase due to Ni. The crystallinity is slightly higher than that of the pure α-MnO_2-SF while displaying a homogeneous distribution of short nanorods (ca. 30 nm), as seen in the SEM (Figure 5a) and TEM (Figure 5b and c). Interestingly, the HRTEM reveals that the lattice fringes have an interplanar distance of 0.5 nm, which is larger than the planar spacing (0.48 nm) of the (200) planes of pure α-MnO_2. This can be due to the swelling of the d spacing by Ni^{2+} substituted in framework sites, in agreement with the XRD refinement showing a = 9.8239 Å and c = 2.8538 Å, which are slightly larger than values for pure α-MnO_2. By characterizing the OER catalytic performance (Figure 6) of the prepared α-MnO_2-HT and Ni/α-MnO_2-SF, we aim to understand how the OER activity was tuned by varying the preparation method and added dopant. Hence, the catalytic performances were evaluated in the same system as mentioned above. A group of representative RDEV curves are shown in Figure 6a. As expected, these three α-MnO_2 materials did not differ a great deal in terms of the overpotential needed to reach a current density of 10 mA cm^{-2} but displayed almost identical current−potential responses. The average overpotentials based on three independent tests are summarized in Figure 6b. For example, α-MnO_2-HT requires η = 0.490 V, whereas Ni/α-MnO_2-SF needs η = 0.508 V, and compared to η = 0.489 V for α-MnO_2-SF. Therefore, the activities do not vary as much for the resulting morphology-changed α-MnO_2 as the phase-changed MnO_2 (AMO, β-MnO_2, and δ-MnO_2). A test using 20 wt % Pt/carbon as an OER catalyst was also performed, and the result is included in Figure 6a. An unsuitable catalytic activity for OER is indicated by the extremely high overpotential, and the 10 mA cm^{-2} target was not reached even with an overpotential close to 1 V. OER performances of two well-known catalysts reported in the literature[2] are also presented in Figure 6b for comparison. Notably, the MnO_x film (alpha-Mn_2O_3), shows a η =0.54 V. Meanwhile, the state-of-the-art OER catalyst 20 wt % Ir/C yields a η =0.38 V. Thus, our α-MnO_2 nanostructures outperformed the superior MnO_x film OER catalyst and other recently reported MnO_2 structures.[3,22]

Although there is still room for improvement in comparison with the best OER catalyst (20 wt % Ir/C), if we take cost into account, the α-MnO_2 materials can still be regarded as a competitive OER electrocatalyst.

Furthermore, we obtained the Tafel plots (Figure 6c) of modified α-MnO_2 materials to compare with that of α-MnO_2-SF. α-MnO_2-HT exhibits a Tafel slope of 87.7 mV dec^{-1}, closest to the Tafel slope for α-MnO_2-SF, both of which are slightly lower than that for Ni/α-MnO_2-SF (107.4 mV dec^{-1}). The results are in agreement with the RDEV results. The small discrepancy in Tafel slope may represent the effect of a modified mechanism of the OER by altering the means of synthesis of the materials.[5] The Tafel slope for α-MnO_2-HT and Ni/α-MnO_2-SF crossed at a relatively low overpotential (E = 0.65 V, Figure 6c, inset), so the performance comparison depends on the regions; e.g., when E < 0.65 V, Ni/α-MnO_2-SF are more active than α-MnO_2-HT, but when E > 0.65 V, the latter is more active.

Finally, we studied the stabilities of α-MnO_2 to clarify the synthetic effects on their stabilities for OER. Chronopotentiometry was performed in extended long-term tests, and the results are illustrated in Figure 6d. The two modified syntheses demonstrate significantly extended lifetimes, and α-MnO_2-HT shows 6.3 h activity before reaching 0.838 V. More strikingly, after the same period of electrolysis time, Ni/α-MnO_2-SF exhibits only 0.775 V, which barely increases. In contrast, it takes 2.4 h for α-MnO_2-SF to reach 0.775 V, and lasts only 2.8 h before reaching 0.838 V from the start. Finally, Ni/α-MnO_2-SF reaches 1.0 V after a 7.9 h continuous test, and outperforms α-MnO_2-SF, which reaches 1.0 V in 3.0 h. As a result, the stabilities of α-MnO_2 follow the trend Ni/α-MnO_2-SF > α-MnO_2-HT > α-MnO_2-SF. This is the first time such stabilities have been reported for MnO_2 materials in OER. In comparison, stabilities of 2 h or less have been reported in similar studies.[28] Our study suggests, despite the α-MnO_2 prepared by hydrothermal synthesis and with Ni dopant by a solvent-free method (both showing close OER activities), that their long-term stabilities are enhanced by these induced modifications, essentially with addition of Ni^{2+} dopants. According to Jaramillo et al., the stability loss of OER could be due to corrosion, material degradation, surface passivation, or many

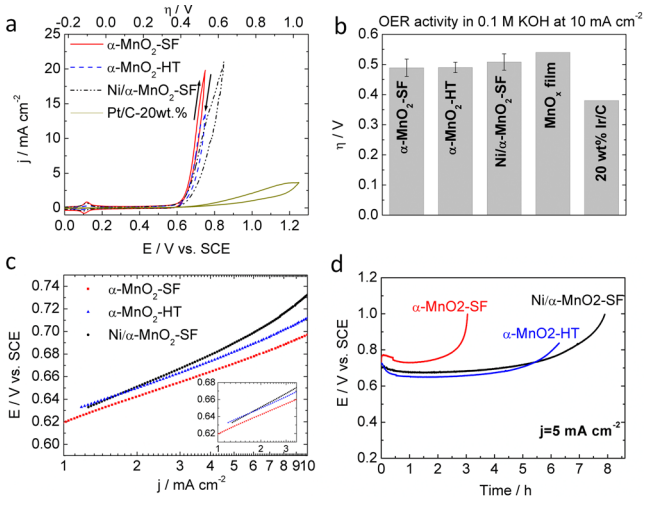

Figure 6. Electrochemical water oxidation performances of three alpha manganese oxides prepared by different methods: (a) Rotating disk electrode voltammogram (RDEV) of oxygen evolution reactions by using α-MnO_2-SF, Ni/α-MnO_2-SF, α-MnO_2-HT, and 20 wt % Pt/C (Sigma-Aldrich) as catalysts, respectively, at a scan rate of 5 mV s^{-1} and a rotation rate of 1600 rpm in 0.1 M KOH. Sweep directions are shown by arrows. (b) Overpotential needs of catalysts by reaching a current density of 10 mA cm^{-2}. The results were compared to the reported data from ref 2 on MnO_x film and state-of-the-art 20 wt % Ir/C OER catalysts. (c) Tafel plots retrieved from RDEVs in part a. (d) Chronopotentiometry curves of α-MnO_2-SF, α-MnO_2-HT, and Ni/α-MnO_2-SF on PG electrodes at a constant current density of 5 mA/cm^2.

dx.doi.org/10.1021/ja505186m | J. Am. Chem. Soc. 2014, 136, 11452−11464

other reasons, though these causes could not be distinguished.[28] This also applies to our study, since we do observe significant material loss under current long-term electrolysis under 0.75 V because of the intense reaction that happens and the oxygen bubbles that come off the electrodes producing strong disturbances on the catalyst coated surfaces. After the stability tests, the remaining catalysts on electrodes were collected and checked using TEM (Figure S9, Supporting Information). The phases were indexed to α-MnO_2, implying the stability of α-MnO_2 under OER conditions, and the activity loss thus could be due to the passivation of the surface caused by the high anodic potential and the vast loss of material. The OER activities for all the manganese oxides are summarized in Table 2, along with the bifunctional MnO_x film catalyst reported in the literature.

2.4. ORR Activities for MnO_2 Nanostructures. In addition, we also conducted ORR experiments using these manganese oxides as catalysts in electrochemical tests. CVs were collected in both Ar- and O_2-saturated 0.1 M KOH solution, at a scan rate of 20 mV s^{-1}; the results are presented in Figure 7. All the CVs conducted in Ar do not display any discernible features, suggesting no reaction happens in the Ar-saturated solution. On the contrary, CVs in the O_2-saturated KOH solution show pronounced oxygen reduction peaks for all the manganese oxide structures. The reduction peaks occur at more positive potentials (ca. −0.15 V) for all three α-MnO_2 structures while occurring at a much more negative potential (ca. −0.35) for δ-MnO_2. Both locations were labeled by drop lines (in red). However, the reduction for β-MnO_2 and AMO occurs in the region between the two marked drop lines. These results reflected that α-MnO_2 catalyzes ORR at lower overpotentials than the other materials, in combination with the observed high peak currents, demonstrating their superior ORR activities. δ-MnO_2 displayed a moderate peak current but has the largest negative overpotential needed to drive ORR, suggesting its inferior catalytic activity in ORR. From CVs, β-MnO_2 and AMO show almost the same peak locations, indicating they both need medium overpotentials to catalyze ORR. Nevertheless, AMO has roughly 2-fold peak currents larger than β-MnO_2, representing AMO's better ORR activity compared to β-MnO_2. Hence, preliminary results from CVs suggest the ORR activity for MnO_2 follows the trend α-MnO_2 > AMO > β-MnO_2 > δ-MnO_2. This finding is in concurrence with other results from the literature, although different preparation methods were employed.[19,35]

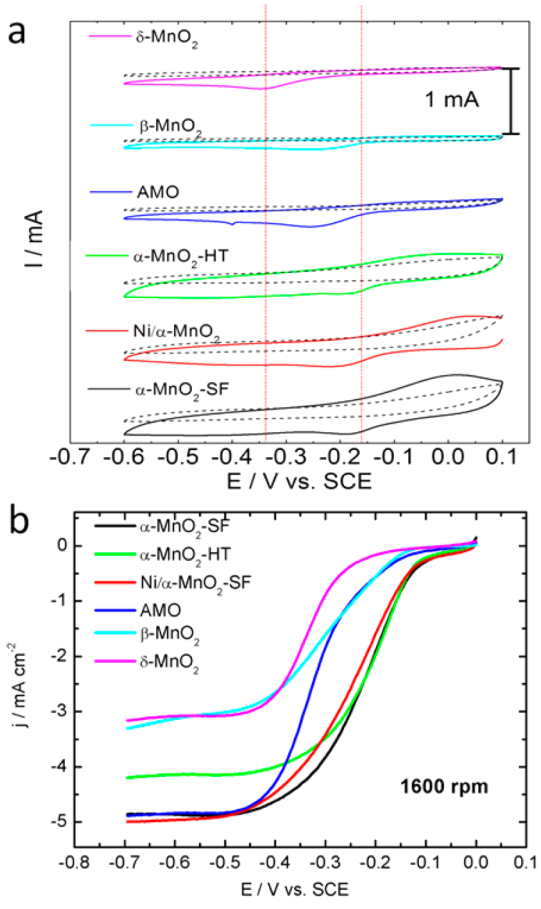

Figure 7. (a) CV curves of manganese oxides measured on a pyrolytic graphite RDE in an Ar-saturated (dotted line) and O_2-saturated (solid line) 0.1 M KOH solution, respectively, at a scan rate of 20 mV s^{-1}. The potential was scanned from 0.1 to −0.6 V vs SCE and then scanned reversibly from −0.6 to 0.1 V. Multiple cycles were swept continuously until reproducible results could be attained. (b) LSV curves of α-MnO_2-SF, α-MnO_2-HT, Ni/α-MnO_2-SF, AMO, β-MnO_2, and δ-MnO_2 studied on RDE electrodes in O_2-saturated 0.1 M KOH solution, at a rotation rate of 1600 rpm with a scan rate of 5 mV s^{-1}.

RDE is useful for getting insight into the kinetics of ORR by eliminating the effects of mass transport. Thus, we further employed RDE to discover the precise kinetics of ORR catalytic activities by rotating the electrodes at various rates, i.e., 400, 900, 1200, 1600, and 2500 rpm. The LSV curves collected under rotating rates of 1600 rpm are shown in Figure 7b (LSV curves for all rotation rates are listed in Figure S10, Supporting Information), and the performance parameters are summarized in Table 3. The onset potential of ORR on α-MnO_2 is at −0.14 to −0.13 V, which is about the same for AMO (−0.14 V) and a little larger for β-MnO_2 (−0.15 V), whereas, for δ-MnO_2, the onset potential increased to −0.30 V. In addition, we also obtained the half-wave potential, which is another figure of merit to study the ORR activities. The half-wave potential for α-MnO_2 falls into a region between −0.20 and −0.24 V. Half-wave potentials of −0.32 and −0.30 V for AMO and β-MnO_2, respectively, are comparable to δ-MnO_2 (−0.34 V). To compare with the performance of materials reported in the literature, we further adopted a current density of 3 mA cm^{-2} as another figure of merit. When reaching this target value, α-MnO_2 (0.74−0.76 V), especially α-MnO_2-SF (0.76 V), shows the closest potential (to standard H_2O/O_2). The performance of this material surpasses that of the MnO_x films (0.73 V), and is close to that for the benchmarking catalyst 20 wt% Pt/C (0.86 V) under similar test conditions. This suggests its superior bifunctionality in both OER and ORR, outperforming the MnO_x film. AMO shows moderate ORR activity that needs 0.67 V to reach 3 mA cm^{-2}. β-MnO_2 and δ-MnO_2 require 0.52 and 0.56 V, respectively, to reach the same value. On the basis of Koutechy−Levich (K−L) plots (Figure S10, Supporting Information), higher current densities were achieved for α-MnO_2 and AMO, which is comparable with previous results on Ag-containing α-MnO_2[31] and other results on α-MnO_2.[19] The electron transfer numbers n were also calculated from K−L plots; the average numbers are 4.2, 3.7, and 3.9 for α-MnO_2-SF, α-MnO_2-HT, and Ni/α-MnO_2-SF, respectively, implying that α-MnO_2 adopts an ideal four-electron transfer mechanism in ORR.[19] In contrast, the n numbers are 2.5, 2.4, and 1.7 for

dx.doi.org/10.1021/ja505186m | J. Am. Chem. Soc. 2014, 136, 11452−11464

Table 3. Summary of the ORR Catalytic Performance Revealed from LSV Curves and K−L Plots

catalyst	E_0[a] (V)	$E_{1/2}$[a] (V)	$E_{j=-3\mathrm{mAcm}^{-2}}$[b] (V)	J_{dl}[a] (mA/mg)	J_k[c] (mA/mg)	n[d]
α-MnO_2-SF	−0.13	−0.22	−0.25 (0.76)	−20.2	40.7	4.2 (4.4)
α-MnO_2-HT	−0.13	−0.20	−0.26 (0.75)	−17.3	36.1	3.7 (3.8)
Ni/α-MnO_2-SF[a]	−0.14	−0.24	−0.27 (0.74)	−20.6	36.7	3.9 (3.8)
AMO	−0.14	−0.32	−0.34 (0.67)	−20.2	43.9	2.5 (1.5)
β-MnO_2	−0.15	−0.30	−0.49 (0.52)	−13.6	12.3	2.4 (2.5)
δ-MnO_2	−0.30	−0.34	−0.45 (0.56)	−13.1	7.9	1.7 (1.2)
MnO_x film[e]	n.a.	n.a.	n.a. (0.73)	n.a.	n.a.	n.a.
20 wt % Pt/C[e]	n.a.	n.a.	n.a. (0.86)	n.a.	n.a.	n.a.

[a]Results based on LSV curves collected on RDE at a rotation rate of 1600 rpm; E_0 versus SCE is the onset potential where ORR starts, which is determined by using the E of the maxima in $d^2i/dE^2 \sim E$; $E_{1/2}$ versus SCE is the half-wave potential; J_{dl} is the diffusion limiting current normalized to the weight of the catalyst (0.04 mg). [b]Potentials versus SCE, and converted to potentials versus RHE shown in parentheses. [c]J_k is the kinetic current density calculated at a potential of −0.3 V; the kinetic current was attained from the intercept of the K−L plots, as shown in Figure S10 (Supporting Information). [d]n is the overall number of electrons transferred per oxygen molecule, which were calculated from K−L plots (based on the average of the electron transfer numbers at −0.2, −0.3, −0.4, and −0.6 V, with n in parentheses showing the electron transfer number at −0.3 V). [e]Results obtained from reference, versus RHE. "n.a." stands for data that are not available from the literature.

AMO, β-MnO_2, and δ-MnO_2, respectively, which suggests a less favored 2 e^- transfer mechanism instead.[19,35]

3. DISCUSSION

Manganese oxides have been thoroughly studied as cheaper substitutes for noble metal catalysts in both ORR and OER. In this study, the activities have been examined by synthesizing pure phase manganese oxide nanostructures referring to the synthetic methods producing the highest activity in the literature.[1,32] AMO, for example, which showed the highest WO activity when using CAN and ruthenium dye as oxidants, and α-MnO_2, prepared by a solid state synthesis, showed superior ORR activity when compared with their counterparts made by hydrothermal and reflux methods. However, their OER activities in electrochemical WO were still unknown. The ORR and OER activities have never been studied together for these two active materials, despite independent studies revealing their excellent activities in OER and ORR, respectively. As such, we explored these materials as bifunctional catalysts in a consistent electrochemical cell, and systematically studied their intrinsic ORR and OER activities and stabilities.

3.1. Materials Property, the Decisive Role of Structure, and Reaction Mechanism. The decisive role of structure on the OER activities has been reported in the literature. For example, a recent study[22] of layered (close to δ-MnO_2) and tunnel manganese oxides (close to γ-MnO_2) points to the layered manganese oxides as having more accessible active sites, i.e., di-μ-oxo-bridged metal ions, likely a universal feature of all electrodeposited WO catalysts using transition metals, such as Mn, Ni, and Co oxides.[53−55] Accordingly, the layered MnO_x presumably is more active than its counterparts with tunnel structure (1 × 1, 1 × 2).[22] However, the activity is also related to the extent of order of the structure. With exceedingly high levels of order for the edge-shared MnO_6 in birnessite (δ-MnO_2), the OER catalytic activities were jeopardized because of a lack of the protonation μ_2-O(H) sites, thus showing limited activity.[22] This is also the case in our study: δ-MnO_2 shows both the lowest OER activities and stabilities. To pursue the effect of order, we studied AMO, an analogue to hexagonal birnessites with cation vacancies, highlighted as a highly disordered stacking of MnO_2 sheets accompanied by poor crystallinity revealed by its XRD pattern (Figure 2). As expected, this more disordered structure displays largely improved activity by reaching 10 mA cm^{-2} at η = 0.59 V, against 0.74 V for well ordered δ-MnO_2 to reach the same current density. This improvement was demonstrated in the chronopotentiometry studies by displaying a longer stability for AMO (450 s) against δ-MnO_2 (87 s). To further exploit the impacts of the various structures that manganese oxides have, β-MnO_2 and α-MnO_2 were investigated in this study as two typical tunnel structured manganese oxides. β-MnO_2 is featured for its corner-shared MnO_6 in its structural unit and forms a small tunnel structure (1 × 1) absent of extra water and cations. Thus, β-MnO_2 has prevalent mono-μ_2-oxo bridges, as opposed to δ-MnO_2, which is dominated by edge-shared MnO_6 consisting of a sizable amount of di-μ_2-oxo bridges between Mn ions. The accessibility to β-MnO_2 is also limited due to small voids in the structure,[43] which further deteriorates the activity. However, many studies showed that low activity was related to both structures due to their highly ordered nature and a shortage of available deprotonation sites to oxidize water. More importantly, we show that OER activity of α-MnO_2 has the highest activity with a low overpotential of 0.49 V to reach 10 mA cm^{-2}, the lowest Tafel slope, and the highest stability (>3 h). On one hand, α-MnO_2 has a distinct structure (2 × 2 tunnel) while eight surrounded MnO_6 units that form a theoretical tunnel size (4.6 Å × 4.6 Å) and hence represents a combination of edge-shared MnO_6 (in the same slab) and corner-shared MnO_6. Another distinct feature of α-MnO_2 lies in the cations (K^+) and water accommodated in its tunnel due to the tunnel size and the necessity to balance the negative charge, thus providing μ_2-oxo-O(H) sites with high accessibilities, not only on the surface but also in the bulk material. On the other hand, this material also has mixed valence states (Mn^{3+}/Mn^{4+}), rendering this system as a superior oxidation catalyst in the previously extensive catalytic study,[17,18] including ORR,[32] which may facilitate the charge transfer in the OER process by following a similar redox cycle between Mn^{3+} and Mn^{4+}.[19] On the basis of the ORR mechanism, we postulate OER (the reverse process of ORR) may follow the reaction paths shown below.

$$4OH^-(aq) - 4e^- \leftrightarrow O_2(g) + 2H_2O(aq) \quad (4)$$

The redox reaction of MnO_2 could proceed by the following paths to promote the OER process:

$$MnO_2 + OH^- - e^- \leftrightarrow MnOOH\cdots O \quad (5)$$

dx.doi.org/10.1021/ja505186m | J. Am. Chem. Soc. 2014, 136, 11452−11464

$$2(\mathrm{MnOOH\cdots O}) \leftrightarrow 2\mathrm{MnOOH} + \mathrm{O_2} \quad (6)$$

$$\mathrm{MnOOH} + \mathrm{OH^-} - \mathrm{e^-} \leftrightarrow \mathrm{MnO_2} + \mathrm{H_2O} \quad (7)$$

On the basis of the proposed OER mechanism, in search of a facile OER catalyst in alkaline medium, feasible catalysts should have the merits of strong adsorption for protons (dissociation of OH^- group) and good ionic and charge transfer abilities. α-MnO_2 has relatively larger tunnel sizes and a great deal of edge-shared MnO_6 (μ_2-oxo-O(H) bridges), which favor the access of water, transportation of ions such as H^+ and O^-, and fast charge transfer. Further investigation of the α-MnO_2 prepared by hydrothermal methods and adding Ni dopant produces little influence on the OER activities by showing very close OER activities. The small decrease on the activity may be due to the long-range order of hydrothermally synthesized α-MnO_2, which shows a larger domain (>2 μm, fibrous) as compared with α-MnO_2-SF (<100 nm, short fibers) which potentially compromised the activity. Second, adding Ni dopant produces a subtle change on the activity due to a varied ratio of Mn^{3+}/Mn^{4+}, thus varying the active sites and conductivity.[56,57] However, these effects resulting from various synthetic methods only adjusted the activity very slightly. The effect of structure is far more determinative and critical on catalyzing OER than the previously claimed surface area effects,[25] which is in line with several recent reports.[22,26]

3.2. Oxidation States, Electrochemical Surface Area (ECSA). We further proceeded to probe oxidation states by using XPS to discover the contribution to the activities of this factor. The relative positions of the $2p_{1/2}$ ($\Delta E_{2p_{1/2}}$) satellite and the magnitude of the 3s multiplet splittings (ΔE_{3s}) were extracted from the experimental results (Table S1 and Figures S12 and S13, Supporting Information). The binding energies (BEs) of Mn $2p_{3/2}$ for all the manganese oxides studied here showed values larger than 642 eV, indicating their valence states are all close to +4.[58,59] This was supported by the magnitude of ΔE_{3s}, which were in the range between 4.4 eV (+4) and 5 eV (+3).[2,60] Moreover, β-MnO_2 and δ-MnO_2 show the lowest ΔE_{3s} values of 4.4 and 4.5 eV, respectively, suggesting their highest oxidation states (ca. +4), which is unfavorable for OERs that are mainly catalyzed by Mn^{3+}.[30,61] Therefore, this explains why these two materials are relatively inert under the electrochemical OER tests. In contrast, three materials of α-MnO_2 structure displayed similar oxidation states, by showing ΔE_{3s} = 4.6–4.7 eV, $\Delta E_{2p_{1/2}}$ = 11.9 eV, and an AOS estimated to be close to 3.7, representing their nature of mixed valencies inclined to enhance the OER activities.[10,12,26] AMO demonstrates an AOS between 3.7 and 3.9, corresponding to its mixed valences including Mn^{3+} residing in between the layers of hexagonal birnessites. These oxidation states actually vary during the electrolysis steps in OER, and were observed in our CV-RDE study similar to other reports.[2,27] In particular, for the cyclic voltammetry of those α-MnO_2 structures, a reversible redox feature (1.1 V vs RHE) was shown in all the OER tests, attributed to transitions between Mn^{3+} and Mn^{4+}. This oxidation phenomenon also happened in the OER catalyzed by the most active oxygenic catalyst $CaMnO_4$ but oxidized by chemical oxidant, hence leading to a similar OER mechanism.[15] However, this is not the case for β-MnO_2 and δ-MnO_2. No redox features were observed. Although AMO did not show obvious features of Mn^{3+}/Mn^{4+}, a broadened feature of such a transition was seen. This is most likely caused by electronic interactions in amorphous materials.[27] To verify the validity of the comparison made between the MnO_x films with our manganese nanostructures, we estimated the electrochemically active surface areas (ECSA) of our three α-MnO_2 materials by integrating the amount of charge responsible for the corresponding Mn^{3+}/Mn^{4+} feature in the CV curves. The results show that α-MnO_2-SF, Ni/α-MnO_2-SF, and α-MnO_2-HT have an ECSA of 3.3, 2.8, and 0.95 cm^2, respectively, compared with 2.8 cm^2 for the MnO_x film.[2] This confirms our results are readily comparable with the study of Jaramillo et al. on a MnO_x film by showing similar ECSA. The relatively larger ECSA shown by the α-MnO_2 (-SF and Ni/-) implies that α-MnO_2 prepared by a solvent-free method created more active sites, benefiting from the nanosized crystallites and high surface areas afforded by this method.

3.3. Charge Transfer Rate Studied by Electrochemical Impedance Spectroscopy (EIS). Ionic and charge transport are crucial factors for performance as efficient electrochemical OER catalysts, due to the mediation role of the manganese oxides played in OER as discussed in section 3.1. Thus, we measured the electrochemical impedance under OER reaction conditions using EIS (Figure 8), aimed at discovering direct

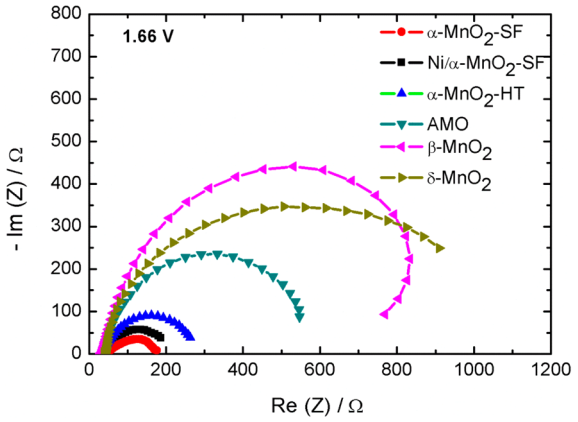

Figure 8. Nyquist plots obtained from EIS measurements in O_2-saturated 0.1 M KOH solution on the manganese oxide modified PG carbon electrodes at an anodic polarization potential of 0.65 V (1.66 V vs RHE).

evidence for the remarkable OER activities controlled by structure activity relations. The resistance shown in the high frequency region is related to the uncompensated solution resistance (R_s, ohmic resistance),[62] which is comparable for all catalysts. The charge transfer resistances were obtained from the fitted equivalent circuit (Figure S14, Supporting Information) and are listed in Table S3 (Supporting Information), and give an interpretation of the reaction kinetics. All the α-MnO_2 structures show much less charge transfer resistance (R_{ct}) ranging from 90 to 210 Ω than AMO which shows 476 Ω. β-MnO_2 had an intermediate charge transfer resistance (613 Ω), and δ-MnO_2 exhibited the largest R_{ct} of 666 Ω. The EIS spectra for the bare PG electrode exhibit an extremely high R_{ct} value of 25 000 Ω, manifesting the effectiveness of applying catalysts. R_{ct} follows the order α-MnO_2-SF < Ni/α-MnO_2-SF < α-MnO_2-HT < AMO < β-MnO_2 < δ-MnO_2, in perfect correlation with the OER (Figures 3 and 5) activity trend implying an inverse relationship.

3.4. Oxygen Desorption Characterization by TPD (Temperature-Programmed Desorption). Given the excellent structure–activity relationship shown in both OER and

dx.doi.org/10.1021/ja505186m | J. Am. Chem. Soc. 2014, 136, 11452–11464

ORR, α-MnO_2 appears to have superior deprotonating activities and fairly good charge transport ability that contributes to the remarkable OER activity. Likewise, an effective catalyst for ORR should have good adsorption ability for O_2, which is the key in the MnO_2 mediated ORR mechanism[63] where uptake of O_2 followed by an electron receptive step to transform O_2 to OH^-/HO_2^- regardless of a $4e^-$ or $2e^-$ pathway[64] are significant. In this regard, we characterized the O_2 adsorption abilities of all the manganese oxide structures by performing O_2 TPD/MS tests (Figure 9).

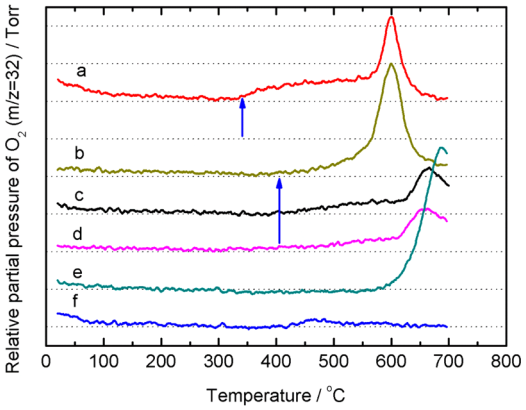

Figure 9. Oxygen temperature-programmed desorption/mass spectrometry (O_2-TPD/MS) profiles of manganese oxide nanostructures: (a) AMO, (b) α-MnO_2-HT, (c) Ni/α-MnO_2-SF, (d) α-MnO_2-SF, (e) β-MnO_2, and (f) δ-MnO_2.

The O_2 TPD profile of AMO exhibits two desorption peaks. The first one spans over 350−550 °C, indicating oxygen adsorbates, and the other distinct peak located above 550 °C represents lattice oxygen.[39,65] In comparison, all the α-MnO_2 materials showed similar desorption regions as AMO, but the first desorption peaks occur at nearly 400 °C, indicating a much stronger oxygen binding ability than AMO.[39] Apart from this, β-MnO_2 and δ-MnO_2 display no or featureless desorption corresponding to adsorbed oxygen, explaining their inferior ORR activities (Figure 7) due to the lowest oxygen adsorption capability. Furthermore, α-MnO_2 prepared by a solvent-free method (with and without Ni) displays nearly overlapping TPD profiles, featuring a wider desorption peak and an increased decomposition temperature (sharp desorption peak at 650 °C) than those for α-MnO_2-HT made by a hydrothermal method. As a result, the ORR activities for α-MnO_2-SF and Ni/α-MnO_2-SF are slightly higher by showing enhanced ORR current densities (Figure 7 and Table 3). Most importantly, the improved thermal stability offered by the solvent-free synthesis could find promising applications under harsh ORR conditions, such as high temperature solid oxide fuel cells.[66]

4. CONCLUSIONS

In summary, manganese oxide nanostructures of various crystal structures were prepared using facile synthetic methods. These materials have been studied systematically as electrocatalysts in both electrochemical oxygen evolution and oxygen reduction reactions in alkaline media. The catalytic performance for both OER and ORR is found to be highly dependent on the crystallographic structure. The OER catalytic activities follow an order of α-MnO_2-SF > AMO > β-MnO_2 > δ-MnO_2. Extensive characterization using XRD, SEM, TEM, BET, XPS, CV, RDEV, Tafel analyses, and constant current study showed the superior OER activity and durability for α-MnO_2-SF, which were attributed to several factors including the following: the abundant μ_2-oxo-O(H) active sites that exist in the edge-shared MnO_6 units analogous to the OEC complex in PS-II, lacking order in large domains (<50 nm), suitable tunnel sizes (0.46 × 0.46 nm^2), and large surface areas (112 m^2/g) affording high accessibility to the water molecule, as well as the efficient charge and ionic transport revealed by EIS. The OER activity for α-MnO_2 outperforms the MnO_x films by showing a lower overpotential of 0.49 V vs 0.54 V to reach 10 mA cm^{-2}, with a facile charge transfer mechanism. An OER study using hydrothermally synthesized α-MnO_2 (nanofiber, >5 μm) and solvent-free α-MnO_2 with Ni^{2+} dopant displayed a comparable OER activity to that of α-MnO_2-SF but exhibited a great deal of improved durability. This verifies the determinative role of the crystallographic structure and provides choices for ameliorating the OER process by controlled syntheses. Finally, ORR activities over these catalysts were studied in the hope of revealing the bifunctionalities of manganese oxides and the structure−activity relations. The catalytic activity for ORR follows the same trend as OER over the manganese oxides due to their different structures. The kinetic studies from K−L plots reveal a $4e^-$ transfer of α-MnO_2 compared to other materials that have $2e^-$ transfer, thus affording exceptional activities by showing enhanced current densities and reduced overpotentials. Ni^{2+} doped α-MnO_2 and α-MnO_2-HT offer similar activities as α-MnO_2-SF (slightly lower for the latter) mainly due to the improved thermal stability and bonding with O_2 adsorbents related to the solvent-free synthesis. This is based on TPR studies over these materials. Our study discovered and highlighted structure-controlled activities of abundant manganese oxides coupled with facile syntheses, and sheds light on the search for accessible environmentally benign OER/ORR bifunctional catalysts with a goal of their applications in solar water splitting, fuel cells, electrolysis, and metal air batteries.

5. EXPERIMENTAL SECTION

5.1. Synthesis. *Amorphous Manganese Oxide (AMO).* AMO was prepared by following synthesis procedures reported in the literature.[1] Typically, 1.58 g of $KMnO_4$ was dissolved in 60 mL of distilled deionized water (DDW), forming a solution, which was then added dropwise to 100 mL of oxalic acid solution (contains 2.28 g of oxalic acid). The resulting mixture was stirred for 2 h at room temperature. Afterward, the resultant slurry was filtered, and the products were washed with DDW and dried at 90 °C overnight.

α-MnO_2 (Na, K) (Tunnel 2 × 2, Cryptomelane). (a) α-MnO_2-SF was synthesized by a solid state method that was first reported by our group,[41] and follows the same procedures as in a recent study:[1] 9 mmol of $Mn(Ac)_2{\cdot}4H_2O$ was mixed together with 6 mmol of $KMnO_4$ (Mn^{2+}:Mn^{7+} = 3:2) in an agate mortar and ground for 20 min. The dark purple colored powder mixture was then transferred to a glass vial, capped, and kept in a 120 °C oven for 4 h. The resulting black fine powder was cooled and washed with distilled deionized water (DDW) five times and then dried at 80 °C overnight. (b) Ni doped α-MnO_2 was synthesized by a similar solvent-free procedure by adding 0.75 mmol of $Ni(NO_3)_2{\cdot}6H_2O$ in the manganese salt mixture, which results in a nominal Ni/Mn ratio of 1:20,[32] and the final sample was denoted as Ni/α-MnO_2-SF. (c) α-MnO_2 was also synthesized by a facile hydrothermal method to study the effect of preparation methods and morphological differences on OER and ORR reactions. The synthesis was done by dissolving 1.7 g of $NaMnO_4{\cdot}H_2O$ and 0.68 g of $MnSO_4{\cdot}H_2O$ in 60 mL of distilled deionized water (DDW). The well dissolved mixture was transferred to a Teflon lined autoclave placed in an oven

dx.doi.org/10.1021/ja505186m | J. Am. Chem. Soc. 2014, 136, 11452−11464

maintained at 240 °C for 4 days. After cooling, the resulting products were decanted and washed by DDW five times using a centrifuge, and then dried at 80 °C overnight. The as prepared sample was denoted as α-MnO_2-HT.

δ-MnO_2 (Layered, Birnessite). K-birnessite was synthesized by dissolving 10 mmol of $KMnO_4$ in 65 mL of DDW. The solution was added to a Teflon-lined autoclave and reacted for 2 days at 220 °C. After cooling, the products were decanted and washed five times using DDW and dried at 80 °C overnight.

β-MnO_2 (Tunnel 1 × 1, Pyrolusite). β-MnO_2 (tunnel 1 × 1, pyrolusite) was synthesized by adding 20 mmol of $MnSO_4$ into a 13 mL solution containing 20 mmol of $NaMnO_4$ (1:1 mol/mol). The mixed solution was loaded in a Teflon-lined autoclave for hydrothermal reaction at 240 °C for 4 days. Then, the autoclave was cooled and the products were washed with DDW and dried at 80 °C overnight. Commercial Pt/carbon (20%) was purchased from Aldrich as a benchmark catalyst.

5.2. Characterization. X-ray diffraction (XRD) data were collected using a Rigaku UltimaIV instrument with Cu Kα radiation (λ = 0.154056 nm) at a beam voltage of 40 kV and a 45 mA beam current. The Brunauer–Emmett–Teller (BET) specific surface areas were determined by nitrogen sorption isotherms that were measured on a Micrometritics ASAP 2010 instrument, to obtain the surface areas and pore volume information. Samples were pre-degassed at 150 °C for 6 h prior to each measurement in order to remove physically adsorbed species. The isotherms for adsorption and desorption were measured at relative pressures (P/P_0) from 0.001 to 0.995 and from 0.995 to 0.001, respectively. X-ray photoelectron spectroscopy (XPS) was done on a PHI model 590 spectrometer with multiprobes (ΦPhysical Electronics Industries Inc.), using Al Kα radiation (λ = 1486.6 eV) as the radiation source. Morphologies were studied using field emission scanning electron microscopy (FE-SEM) (FEI Nova NanoSEM 450) at an accelerating voltage of 2.0 kV. Energy dispersive X-ray spectroscopy (EDX) was performed on an Oxford Aztec Energy microanalysis system with an X-Max 80 silicon drift detector. High resolution transmission electron microscopy (HR-TEM) images were collected using a JEOL 2010 FasTEM with an accelerating voltage of 200 kV. O_2 temperature-programmed desorption mass spectrometry studies (O_2-TPD/MS) were performed to measure the adsorption ability of O_2 for each catalyst. Typically, 100 mg of catalyst was packed inside a quartz tube held by quartz wool on both sides and loaded into a homemade tube furnace with a temperature controller. The catalyst was pretreated by flowing Ar (UHP) at a flow rate of 200 cm^3 min^{-1} (sccm) at 150 °C. Adsorption of O_2 was carried out at room temperature by flowing O_2 (ultrahigh purity) at the same flow rate for 1 h. The catalyst was subsequently purged with Ar to remove the surface absorbed O_2 at room temperature (R.T.). Desorption was performed by heating the catalysts under a constant Ar flow (200 sccm) from R.T. to 700 °C at an increasing ramp rate of 10 °C min^{-1}. The effluents were monitored by an e-Vision + residual gas analyzer MKS coupled with a quadruple mass selective detector.

5.3. Electrochemical Studies. *OER.* We studied the OER activities using cyclic voltammetry (CV) in an RDE configuration. All the CVs were *iR*-compensated (100%) and measured in a three-electrode electrochemical cell on a CHI 660A electrochemical workstation at ambient temperature (22 ± 2 °C) and 1600 rpm, with a sweep rate of 5 mV s^{-1}. The cell setup consisted of a working electrode (pyrolytic graphite carbon) coated with the sample in the form of a thin film, a SCE reference electrode, a Pt counter electrode, and a 0.1 M KOH solution as the electrolyte. The working electrode was prepared as follows: 10 mg of active material sample and 10 mg of carbon (VulcanXC-72) were dispersed in a mixture of deionized distilled water (DDW) and isopropanol (4 mL:1 mL) and sonicated for 3 min, followed by adding 20 μL of polytetrafluoroethylene (PTFE) solution (60% in water, Sigma) and sonicating for 5 min to form a suspension. A 20 μL suspension was deposited onto a pyrolytic graphite substrate using a micropipette. The catalyst loadings were 0.204 mg/cm^2. During the experiments, the three electrodes were placed into the electrolyte. The cell was purged with O_2 (zero grade, Airgas) for 30 min to saturate the electrolyte, and the O_2 flow was maintained over the solution during the test. An initial scan was done by sweeping from 0 to 0.7–0.9 V vs SCE for three continuous cycles. The first cycle was used to reveal the intrinsic properties of the catalysts.

ORR. Cyclic voltammetry (CV) was performed in the same three-electrode configuration as mentioned above. The cell was purged with O_2 (UHP, Airgas) for 30 min to saturate the electrolyte followed by an initial scan to record the electrochemical oxygen reduction activities of the materials at a scan rate of 25 mV/s. Then, the ORR activities were obtained by conducting more scans until a reproducible scan was obtained, and O_2 was kept flowing over the surface of the electrolyte during the test process. The background currents were also collected by purging the cell with Ar (g) for 30 min and then measuring the CVs under the same conditions as was used in O_2. The Ar flow was maintained during the background collection. All experiments were conducted at ambient temperature (22 ± 2 °C).

Linear Sweep Voltammetry-Rotating Disk Electrodes (LSV-RDEs). Linear sweep voltammograms were measured on rotating disk electrodes (RDEs) with the aid of RDEV (Pine Instruments). The RDEV was measured by rotating the RDEs at various rotating rates, (400, 900, 1200, 1600, 2000, and 2500 rpm) and at a scan rate of 5 mV s^{-1} starting from −0.1 to −0.7 V (versus SCE). The cell used the same configuration as mentioned above. Before use, all the PG carbon electrodes were abraded with 600 grit SiC paper under wet conditions and then washed and ultrasonicated for 30 s, with drying at 80 °C for 20 min. The catalyst suspension was casted and then was allowed to dry overnight in a fume hood. The catalyst loadings were 0.204 mg/cm^2. Similar to the CV experiments, O_2 was purged in the electrolyte for 30 min before each test, and was kept flowing over the electrolyte during the tests.

Chronopotentiometry. A chronopotentiometric test was done in the same three-electrode cell using O_2-saturated 0.1 M KOH as the electrolyte with continuous O_2 flowing over the electrolyte during the test, and the catalyst coated electrodes were rotated at 1600 rpm. A continuous current density of 5 mA/cm^2 was used for the anodic reaction. The potential window was set between 0.75 and 1.2 V (versus SCE), which is in the OER active potential window, determined from three cycles of CV before the tests were started. Note all the CV and LSV tests were 100% *iR* compensated, except for the chronopotentiometric test where no *iR*-compensation was applied.

Electrochemical Impedance Spectroscopy (EIS). The EIS test was conducted using a CHI 660A electrochemical workstation. The measurements were carried out in O_2-saturated 0.1 M KOH solution on the manganese oxide coated PG carbon electrodes at an anodic polarization potential of 0.65 V vs SCE (1.66 V vs RHE). The spectra were collected in a frequency range of 0.1–10^5 Hz with an amplitude of 5 mV.

5.4. Calculation. The mass activity (A g^{-1}) was calculated on the basis of the catalyst loading m = 0.204 mg cm^{-2} and the measured current density j (mA cm^{-2}) at η = 0.45 V by

$$\text{mass activity} = \frac{j}{m}$$

The turnover frequency (TOF) was calculated on the basis of the catalyst loading m = 0.204 mg cm^{-2}, and the measured current density j (mA cm^{-2}) at η = 0.45 V by

$$\text{TOF} = \frac{j \cdot A}{4nF}$$

j is the measured current density (mA cm^{-2}) at η = 0.45 V, A is the geometric area of the PG electrode, n is the mole number of the coated catalysts, and F is the Faraday constant (96 500 C mol^{-1}).[67]

■ ASSOCIATED CONTENT

Ⓢ Supporting Information

Figures S1–S14 and Tables S1–S3 include information for oxygen electrode activities, CV curves for OER, SEM images, TEM images for catalysts before and after reaction, LSV curves and corresponding Koutechy–Levich (K–L) plots, XPS

spectra, AOS, the calculation of electrochemically active surface areas, and EIS fitting results. This material is available free of charge via the Internet at http://pubs.acs.org.

AUTHOR INFORMATION

Corresponding Author

steven.suib@uconn.edu

Notes

The authors declare no competing financial interest.

ACKNOWLEDGMENTS

The authors would like to thank U.S. Department of Energy, Office of Basic Energy Sciences, Division of Chemical, Geochemical and Biological Sciences (under grant DE-FG02-86ER13622.A000), and Honda for funding this research. We would like to thank Dr. Ray Joesten for help in analyzing the crystal structures. We thank the Institute of Material Science, University of Connecticut, for access to the XPS instrument. We would like to thank Dr. James Rusling for use of CHI660A and Pine Instruments RDEV apparatus. We thank Dr. John Ong and Daniel Daleb for the creative mechanical design and processing of the electrode holders. We also thank Drs. Frank Galasso, Heng Zhang, Yun Zhang, and Junkai He for many help discussions. Y.M. thanks Ms. Ge Mu and Karen Ren, staff at the UCONN writing center, for help in preparing the manuscript.

REFERENCES

(1) Iyer, A.; Del-Pilar, J.; King'ondu, C. K.; Kissel, E.; Garces, H. F.; Huang, H.; El-Sawy, A. M.; Dutta, P. K.; Suib, S. L. *J. Phys. Chem. C* **2012**, *116*, 6474−6483.

(2) Gorlin, Y.; Jaramillo, T. F. *J. Am. Chem. Soc.* **2010**, *132*, 13612−13614.

(3) Fekete, M.; Hocking, R. K.; Chang, S. L.; Italiano, C.; Patti, A. F.; Arena, F.; Spiccia, L. *Energy Environ. Sci.* **2013**, *6*, 2222−2232.

(4) Liao, L.; Zhang, Q.; Su, Z.; Zhao, Z.; Wang, Y.; Li, Y.; Lu, X.; Wei, D.; Feng, G.; Yu, Q. *Nat. Nanotechnol.* **2014**, *9*, 69−73.

(5) Walter, M. G.; Warren, E. L.; McKone, J. R.; Boettcher, S. W.; Mi, Q.; Santori, E. A.; Lewis, N. S. *Chem. Rev.* **2010**, *110*, 6446−6473.

(6) Suntivich, J.; May, K. J.; Gasteiger, H. A.; Goodenough, J. B.; Shao-Horn, Y. *Science* **2011**, *334*, 1383−1385.

(7) Lee, Y.; Suntivich, J.; May, K. J.; Perry, E. E.; Shao-Horn, Y. *J. Phys. Chem. Lett.* **2012**, *3*, 399−404.

(8) Mukhopadhyay, S.; Mandal, S. K.; Bhaduri, S.; Armstrong, W. H. *Chem. Rev.* **2004**, *104*, 3981−4026.

(9) Ferreira, K. N.; Iverson, T. M.; Maghlaoui, K.; Barber, J.; Iwata, S. *Science* **2004**, *303*, 1831−1838.

(10) Najafpour, M. M.; Ehrenberg, T.; Wiechen, M.; Kurz, P. *Angew. Chem., Int. Ed.* **2010**, *49*, 2233−2237.

(11) Yagi, M.; Narita, K. *J. Am. Chem. Soc.* **2004**, *126*, 8084−8085.

(12) Kanady, J. S.; Tsui, E. Y.; Day, M. W.; Agapie, T. *Science* **2011**, *333*, 733−736.

(13) Han, X.; Hu, Y.; Yang, J.; Cheng, F.; Chen, J. *Chem. Commun.* **2014**, *50*, 1497−1499.

(14) Singh, A.; Hocking, R. K.; Chang, S. L. Y.; George, B. M.; Fehr, M.; Lips, K.; Schnegg, A.; Spiccia, L. *Chem. Mater.* **2013**, *25*, 1098−1108.

(15) Najafpour, M. M.; Allakhverdiev, S. I. *Int. J. Hydrogen Energy* **2012**, *37*, 8753−8764.

(16) Robinson, D. M.; Go, Y. B.; Mui, M.; Gardner, G.; Zhang, Z.; Mastrogiovanni, D.; Garfunkel, E.; Li, J.; Greenblatt, M.; Dismukes, G. C. *J. Am. Chem. Soc.* **2013**, *135*, 3494−3501.

(17) Suib, S. L. *Acc. Chem. Res.* **2008**, *41*, 479−487.

(18) Suib, S. L. *J. Mater. Chem.* **2008**, *18*, 1623−1631.

(19) Cheng, F.; Su, Y.; Liang, J.; Tao, Z.; Chen, J. *Chem. Mater.* **2010**, *22*, 898−905.

(20) Toupin, M.; Brousse, T.; Bélanger, D. *Chem. Mater.* **2004**, *16*, 3184−3190.

(21) Devaraj, S.; Munichandraiah, N. *J. Phys. Chem. C* **2008**, *112*, 4406−4417.

(22) Bergmann, A.; Zaharieva, I.; Dau, H.; Strasser, P. *Energy Environ. Sci.* **2013**, *6*, 2745−2755.

(23) Gorlin, Y.; Lassalle-Kaiser, B.; Benck, J. D.; Gul, S.; Webb, S. M.; Yachandra, V. K.; Yano, J.; Jaramillo, T. F. *J. Am. Chem. Soc.* **2013**, *135*, 8525−8534.

(24) Boppana, V. B. R.; Yusuf, S.; Hutchings, G. S.; Jiao, F. *Adv. Funct. Mater.* **2013**, *23*, 878−884.

(25) Boppana, V. B. R.; Jiao, F. *Chem. Commun.* **2011**, *47*, 8973−8975.

(26) Zaharieva, I.; Najafpour, M. M.; Wiechen, M.; Haumann, M.; Kurz, P.; Dau, H. *Energy Environ. Sci.* **2011**, *4*, 2400−2408.

(27) Zaharieva, I.; Chernev, P.; Risch, M.; Klingan, K.; Kohlhoff, M.; Fischer, A.; Dau, H. *Energy Environ. Sci.* **2012**, *5*, 7081−7089.

(28) McCrory, C. C.; Jung, S.; Peters, J. C.; Jaramillo, T. F. *J. Am. Chem. Soc.* **2013**, *135*, 16977−16987.

(29) Smith, R. D.; Prévot, M. S.; Fagan, R. D.; Zhang, Z.; Sedach, P. A.; Siu, M. K. J.; Trudel, S.; Berlinguette, C. P. *Science* **2013**, *340*, 60−63.

(30) Takashima, T.; Hashimoto, K.; Nakamura, R. *J. Am. Chem. Soc.* **2012**, *134*, 1519−1527.

(31) Huang, H.; Meng, Y.; Labonte, A.; Dobley, A.; Suib, S. L. *J. Phys. Chem. C* **2013**, *117*, 25352−25359.

(32) Benbow, E. M.; Kelly, S. P.; Zhao, L.; Reutenauer, J. W.; Suib, S. L. *J. Phys. Chem. C* **2011**, *115*, 22009−22017.

(33) Suntivich, J.; Gasteiger, H. A.; Yabuuchi, N.; Nakanishi, H.; Goodenough, J. B.; Shao-Horn, Y. *Nat. Chem.* **2011**, *3*, 546−550.

(34) Liu, Y.; Mustain, W. E. *J. Am. Chem. Soc.* **2013**, *135*, 530−533.

(35) Xiao, W.; Wang, D.; Lou, X. W. *J. Phys. Chem. C* **2009**, *114*, 1694−1700.

(36) Chen, G.; Bare, S. R.; Mallouk, T. E. *J. Electrochem. Soc.* **2002**, *149*, A1092−A1099.

(37) Chen, Z.; Yu, A.; Ahmed, R.; Wang, H.; Li, H.; Chen, Z. *Electrochim. Acta* **2012**, *69*, 295−300.

(38) Truong, T. T.; Liu, Y.; Ren, Y.; Trahey, L.; Sun, Y. *ACS Nano* **2012**, *6*, 8067−8077.

(39) Cheng, F.; Shen, J.; Peng, B.; Pan, Y.; Tao, Z.; Chen, J. *Nat. Chem.* **2011**, *3*, 79−84.

(40) Lu, Y.-C.; Xu, Z.; Gasteiger, H. A.; Chen, S.; Hamad-Schifferli, K.; Shao-Horn, Y. *J. Am. Chem. Soc.* **2010**, *132*, 12170−12171.

(41) Ding, Y.-s.; Shen, X.-f.; Sithambaram, S.; Gomez, S.; Kumar, R.; Crisostomo, V. M. B.; Suib, S. L.; Aindow. *Chem. Mater.* **2005**, *17*, 5382−5389.

(42) Huang, H.; Chen, C.-H.; Xu, L.; Genuino, H.; Garcia-Martinez, J.; Garces, H. F.; Jin, L.; Kithongo, C. K. o.; Suib, S. L. *Chem. Commun.* **2010**, *46*, 5945−5947.

(43) Duan, X.; Yang, J.; Gao, H.; Ma, J.; Jiao, L.; Zheng, W. *CrystEngComm* **2012**, *14*, 4196−4204.

(44) Yeager, M.; Du, W.; Si, R.; Su, D.; Marinković, N.; Teng, X. *J. Phys. Chem. C* **2012**, *116*, 20173−20181.

(45) Rossouw, M.; Liles, D.; Thackeray, M.; David, W.; Hull, S. *Mater. Res. Bull.* **1992**, *27*, 221−230.

(46) Hill, L. I.; Verbaere, A.; Guyomard, D. *J. New Mater. Electrochem. Syst.* **2002**, *5*, 129−134.

(47) Jin, L.; Xu, L.; Morein, C.; Chen, C. h.; Lai, M.; Dharmarathna, S.; Dobley, A.; Suib, S. L. *Adv. Funct. Mater.* **2010**, *20*, 3373−3382.

(48) Kavakli, C.; Meini, S.; Harzer, G.; Tsiouvaras, N.; Piana, M.; Siebel, A.; Garsuch, A.; Gasteiger, H. A.; Herranz, J. *ChemCatChem* **2013**, *5*, 3358−3373.

(49) Trahey, L.; Karan, N. K.; Chan, M. K.; Lu, J.; Ren, Y.; Greeley, J.; Balasubramanian, M.; Burrell, A. K.; Curtiss, L. A.; Thackeray, M. M. *Adv. Energy Mater.* **2013**, *3*, 75−84.

(50) Li, W. N.; Yuan, J.; Shen, X. F.; Gomez-Mower, S.; Xu, L. P.; Sithambaram, S.; Aindow, M.; Suib, S. L. *Adv. Funct. Mater.* **2006**, *16*, 1247−1253.

(51) Meng, Y.; Genuino, H. C.; Kuo, C.-H.; Huang, H.; Chen, S.-Y.; Zhang, L.; Rossi, A.; Suib, S. L. *J. Am. Chem. Soc.* **2013**, *135*, 8594−8605.
(52) Hu, J. *Int. J. Hydrogen Energy* **2004**, *29*, 791−797.
(53) Gerken, J. B.; McAlpin, J. G.; Chen, J. Y.; Rigsby, M. L.; Casey, W. H.; Britt, R. D.; Stahl, S. S. *J. Am. Chem. Soc.* **2011**, *133*, 14431−14442.
(54) Risch, M.; Khare, V.; Zaharieva, I.; Gerencser, L.; Chernev, P.; Dau, H. *J. Am. Chem. Soc.* **2009**, *131*, 6936−6937.
(55) Risch, M.; Klingan, K.; Heidkamp, J.; Ehrenberg, D.; Chernev, P.; Zaharieva, I.; Dau, H. *Chem. Commun.* **2011**, *47*, 11912−11914.
(56) De Guzman, R. N.; Awaluddin, A.; Shen, Y.-F.; Tian, Z. R.; Suib, S. L.; Ching, S.; O'Young, C.-L. *Chem. Mater.* **1995**, *7*, 1286−1292.
(57) Lee, J.-S.; Lee, T.; Song, H.-K.; Cho, J.; Kim, B.-S. *Energy Environ. Sci.* **2011**, *4*, 4148−4154.
(58) Genuino, H. C.; Meng, Y.; Horvath, D. T.; Kuo, C. H.; Seraji, M. S.; Morey, A. M.; Joesten, R. L.; Suib, S. L. *ChemCatChem* **2013**, *5*, 2306−2317.
(59) Özacar, M.; Poyraz, A. S.; Genuino, H. C.; Kuo, C.-H.; Meng, Y.; Suib, S. L. *Appl. Catal., A* **2013**, *462*, 64−74.
(60) Toupin, M.; Brousse, T.; Bélanger, D. *Chem. Mater.* **2002**, *14*, 3946−3952.
(61) Maitra, U.; Naidu, B.; Govindaraj, A.; Rao, C. *Proc. Natl. Acad. Sci. U. S. A.* **2013**, *110*, 11704−11707.
(62) He, Z.; Mansfeld, F. *Energy Environ. Sci.* **2009**, *2*, 215−219.
(63) Lima, F. H. B.; Calegaro, M. L.; Ticianelli, E. A. *Electrochim. Acta* **2007**, *52*, 3732−3738.
(64) Mao, L.; Zhang, D.; Sotomura, T.; Nakatsu, K.; Koshiba, N.; Ohsaka, T. *Electrochim. Acta* **2003**, *48*, 1015−1021.
(65) Iwamoto, M.; Yoda, Y.; Yamazoe, N.; Seiyama, T. *J. Phys. Chem.* **1978**, *82*, 2564−2570.
(66) Aricò, A. S.; Bruce, P.; Scrosati, B.; Tarascon, J.-M.; Van Schalkwijk, W. *Nat. Mater.* **2005**, *4*, 366−377.
(67) Gao, M.; Sheng, W.; Zhuang, Z.; Fang, Q.; Gu, S.; Jiang, J.; Yan, Y. *J. Am. Chem. Soc.* **2014**, *136*, 7077−7084.